

Article

Short- and Long-Range Microparticle Transport on Permalloy Disk Arrays in Time-Varying Magnetic Fields

Gregory Butler Vieira *, Eliza Howard, Dung Hoang, Ryan Simms, David Alden Raymond and Edward Thomas Cullom

Department of Physics, Rhodes College, Memphis, TN 38112, USA; howec-23@rhodes.edu (E.H.); hoadh-23@rhodes.edu (D.H.); simrt-23@rhodes.edu (R.S.); daraymond31@gmail.com (D.A.R.); thomascullom@att.net (E.T.C.)

* Correspondence: vieirag@rhodes.edu

Abstract: We investigate maneuvering superparamagnetic microparticles, or beads, in a remotely-controlled, automated way across arrays of few-micron-diameter permalloy disks. This technique is potentially useful for applying tunable forces to or for sorting biological structures that can be attached to magnetic beads, for example nucleic acids, proteins, or cells. The particle manipulation method being investigated relies on a combination of stray fields emanating from permalloy disks as well as time-varying externally applied magnetic fields. Unlike previous work, we closely examine particle motion during a capture, rotate, and controlled repulsion mechanism for particle transport. We measure particle velocities during short-range motion—the controlled repulsion of a bead from one disk toward another—and compare this motion to a simulation based on stray fields from disk edges. We also observe the phase-slipping and phase-locked motion of particles engaging in long-range transport in this manipulation scheme.



Citation: Vieira, G.B.; Howard, E.; Hoang, D.; Simms, R.; Raymond, D.A.; Cullom, E.T. Short- and Long-Range Microparticle Transport on Permalloy Disk Arrays in Time-Varying Magnetic Fields. *Magnetochemistry* **2021**, *7*, 120. <https://doi.org/10.3390/magnetochemistry7080120>

Academic Editor: Adam J. Hauser

Received: 10 May 2021

Accepted: 1 July 2021

Published: 23 August 2021

Publisher's Note: MDPI stays neutral with regard to jurisdictional claims in published maps and institutional affiliations.



Copyright: © 2021 by the authors. Licensee MDPI, Basel, Switzerland. This article is an open access article distributed under the terms and conditions of the Creative Commons Attribution (CC BY) license (<https://creativecommons.org/licenses/by/4.0/>).

Keywords: patterned magnetic thin films; magnetic microparticles; superparamagnetism

1. Introduction

Spherical superparamagnetic microscale particles, polystyrene spheres encasing sub-100 nm iron oxide nanoparticles, are commonly used for scientific and medical applications for the isolation of known entities from mixtures. This is useful, for example, for sorting rare cells such as circulating tumor cells from a mixture [1,2] or for isolating and purifying known nucleic acid fragments for downstream amplification, used in the detection of diseases such as coronavirus [3]. Often, the manipulation is done with macroscopic, hand-held permanent magnets. However, there has been a recent development of manipulation schemes in conjunction with microscopic surface-patterned magnetic materials, with particle motion controlled by externally-varied magnetic fields [4–8]. These developments in bead trapping and manipulation allow for automated and programmable particle motion, the micro- or nanoscale precision of particle trapping locations, and remotely tunable forces [9]. Patterned structures can be built into microfluidic devices where sorting, isolation, or purification steps, usually done at a macroscopic scale, can be done in lab-on-chip environments with minimal fluid consumption.

Work has been done in measuring and modeling the behavior of particle motion on patterned circular structures [6,9–12], showing motion that exhibits (1) a linear response to an increasing frequency at low field frequencies, and (2) a sluggish motion at high field frequencies, known in the literature as (1) phase-locked and (2) phase-slipping motion [4]. This behavior has been observed for motion across many magnetic structures [4] and for looping beads [6,11,12]. Understanding this behavior may prove useful for biomedical applications, for example for the detection of targeted analytes such as proteins or nucleic acid fragments. Recent work has shown differences in the phase-locked and phase-slipping motion of beads depending on the presence or absence of a specific target analyte that links

beads into doublets or aggregates [7,13]. As such, closely monitoring bead motion serves as a highly sensitive means of biomolecule detection. Obtaining a firm understanding of particle dynamics and creating models to describe bead motion is essential to developing these and similar techniques. Furthermore, investigating bead motion experimentally and modeling bead behavior can yield measurements of physical properties associated with the beads, for example the magnetic susceptibilities of individual beads at low field strengths.

In this paper, we investigate an under-studied method of chip-based particle transport in which beads are captured at a magnetic disk edge, rotated around the disk periphery with in-plane fields, and repelled in a controlled manner from the disk to an adjacent disk using out-of-plane fields. This manipulation method is directed by small (<60 Oersted) externally applied fields and allows not just for unidirectional long-range motion but also for flexible trajectories that experimenters can control in real time [5]. We investigate microparticle trapping (Figure 1) and motion (Figure 2) that include rotation around permalloy disks and disk-to-disk hopping, a versatile manipulation scheme that allows for the application of forces to many particles simultaneously.

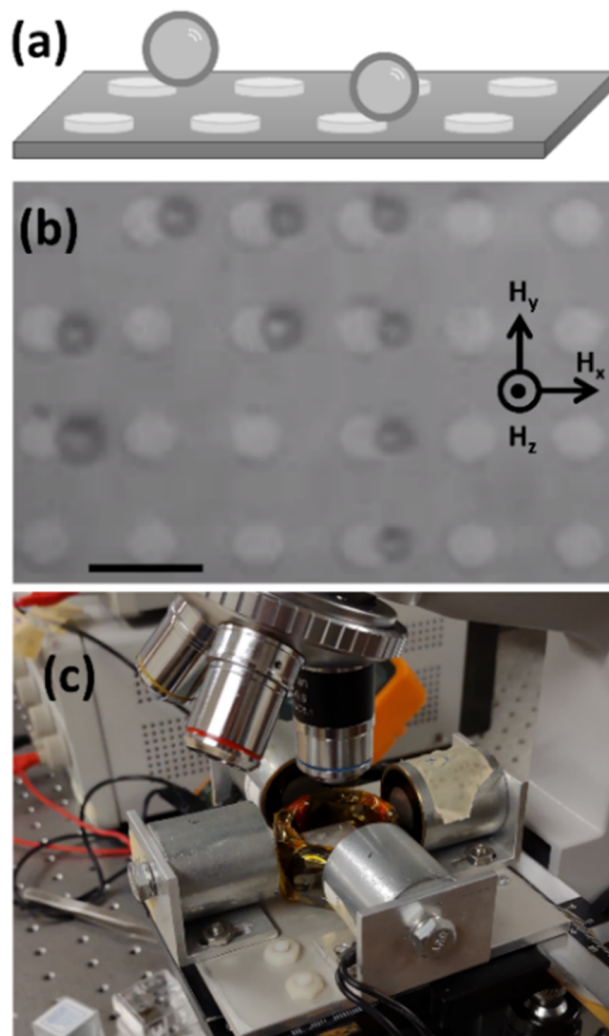


Figure 1. (a) Cartoon of magnetic beads trapped at the peripheries of permalloy magnet disks. (b) Light microscope image of trapped particles. Scale bar: 10 microns. (c) Electromagnets used for generating in-plane and out-of-plane fields.

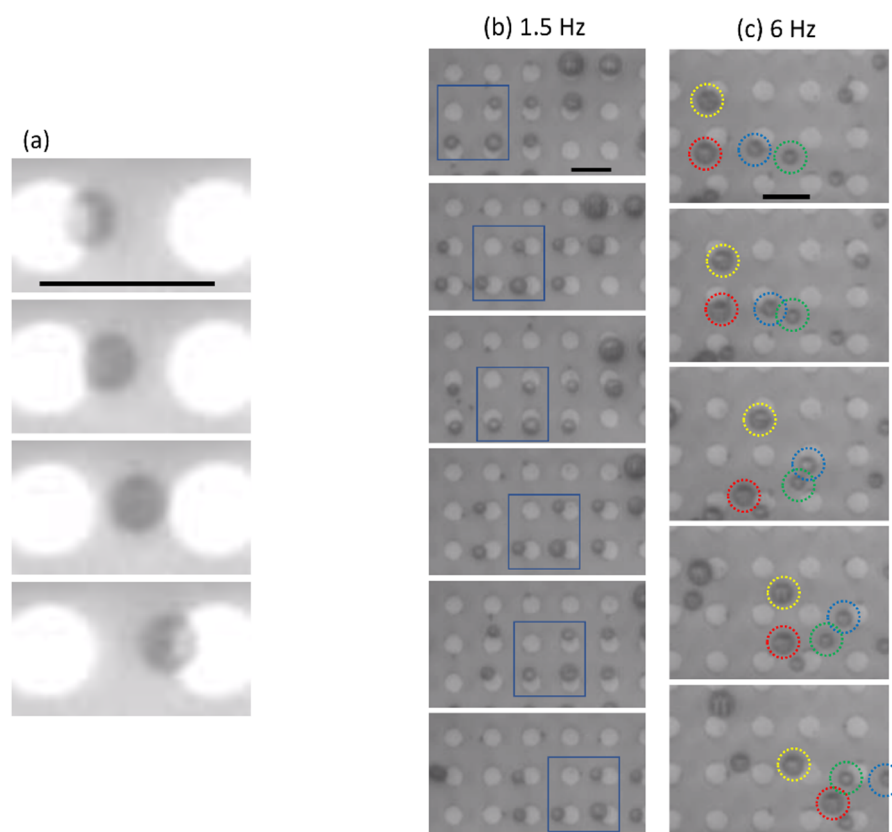


Figure 2. (a) Short range microparticle (dark gray) hopping from permalloy disk (white) to adjacent disk. Particle hopping is initiated by the abrupt direction switching of an out-of-plane magnetic field. (b,c) Particle manipulation across several disks. The mechanism by which long-range motion occurs is detailed in the materials and methods. (b) Low-frequency phase-locked motion using a cycling magnetic field frequency of 1.5 Hz. All particles move synchronously; an example is shown in the blue boxes. (c) High-frequency phase-slipping motion, where rightward motion still occurs, but the motion is not synchronous, as indicated by the particles in multicolored circles. The motion of the particles is no longer synchronous with other particles or with the field. All particles in this figure are Spherotech PMS-20-10, PMS-30-10, or PMS-40-10. Scale bar: 10 microns.

The particles used in this study are Invitrogen Dynabeads M-270 Carboxylic Acid (ThermoFisher, Waltham, MA, USA) and Spherotech PMS-20-10, PMS-30-10, and PMS-40-10 (Spherotech, Lake Forest, IL, USA). Dynabeads are polystyrene beads with an even dispersion of maghemite and magnetite throughout, containing an iron concentration of 12% by weight [14]. Spherotech particles are polystyrene with magnetite at a concentration of 6-8% by weight [15].

To better understand the motion of superparamagnetic microparticles on surfaces, we investigated two regimes of particle motion on surface-based disk arrays: short-range disk-to-disk hopping (~4 microns) and long-range transport (~100 microns). We observe short-range motion with responses to experimental considerations, for example hop time vs. external field magnitude, that can be explained by a model where fields are calculated as emanating from disk edges. We also observe phase-locked and phase-slipping motion, but note differences between our observations as compared to models and similar results in the literature.

2. Results

2.1. Short Range

An example of a disk-to-disk hop is shown in Figure 2a and Video S1. An example of disk position and disk velocities vs. time for a single hop is shown in Figure 3. During

disk-to-disk hops, particles exhibited instantaneous velocities of 20 to 200 microns per second depending on the experimental conditions, but the particle velocity varied over the duration of the hop. The highest particle speeds were generally seen at the beginning and end of each hop (immediately after leaving one disk and immediately before capture by the adjacent disk), consistent with the highest field gradients being located at the disk edges. The particle speed increases and the jump time decreases with an increasing external out-of-plane field H_z .

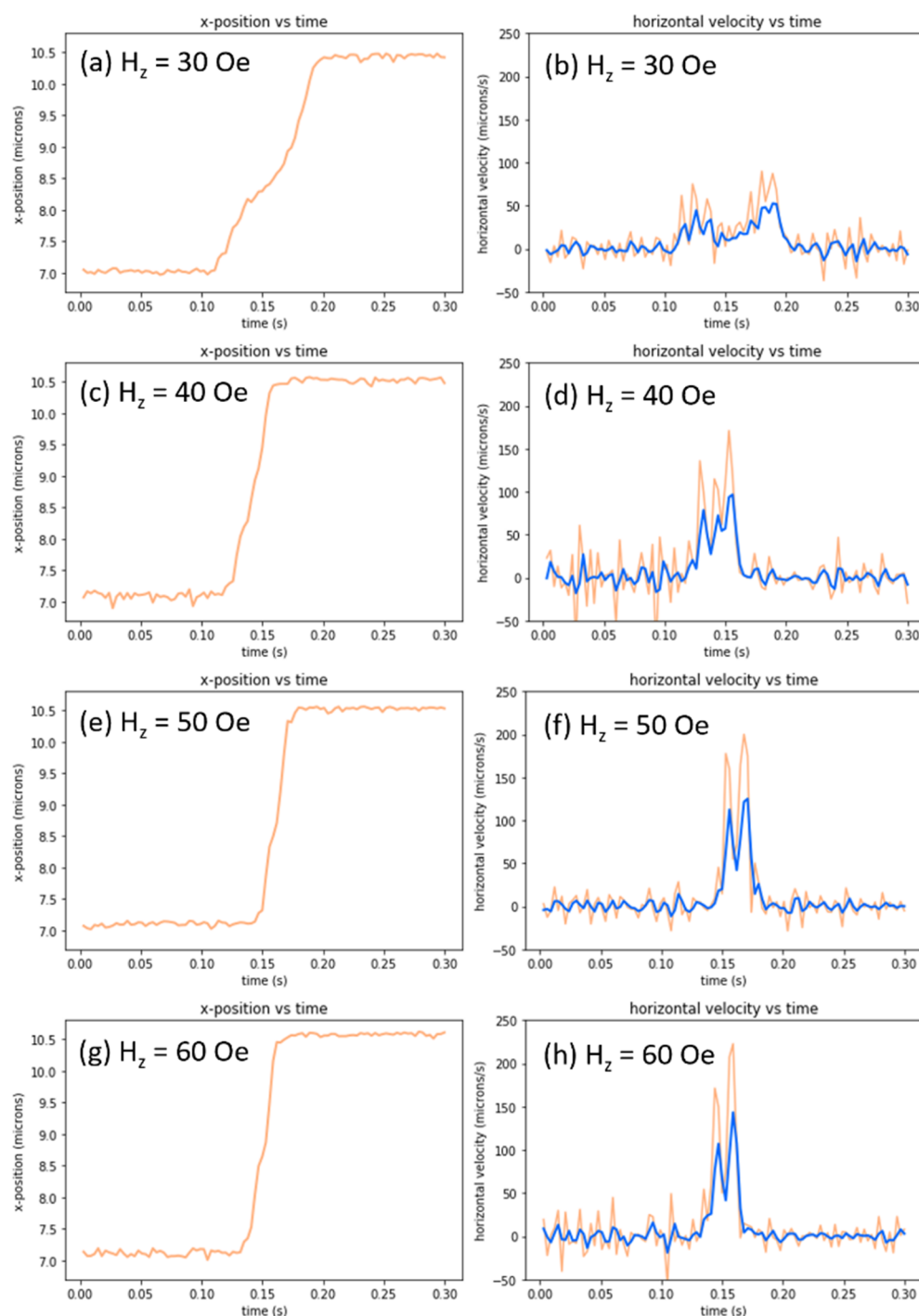


Figure 3. Short-range hopping position vs. time and velocity vs. time graphs for Dynabeads M-270 particles for switching out-of-plane fields H_z of 30 Oe (a,b), 40 Oe (c,d), 50 Oe (e,f), and 60 Oe (g,h). Three-frame average velocities are shown in blue. For all graphs, the in-plane field $H_x = 35$ Oe.

To illustrate how particle hopping characteristics vary with external fields, the time needed for a hop (distance = 3.8–4.0 microns) is compared to the out-of-plane field H_z , while the in-plane field H_x is held at a constant 35 Oe. For an increased H_z , the repulsive force pushing the bead from the disk and pulling the bead to the subsequent disk increases, so the hop time is lower, as seen in Figure 4a. The data were fit with the model described in the Materials and Methods section (blue line). For graphs showing Dynabead M-270 particles, the magnetic susceptibility χ used for the simulation was 0.9, and for the graphs showing Spherotech particles, χ was 0.34. The strength of the source of the magnetic fields λ_0 , as defined in Materials and Methods, was 3.5 mA for the simulations for both types of bead, as the same magnetic disk geometry and material were used for both.

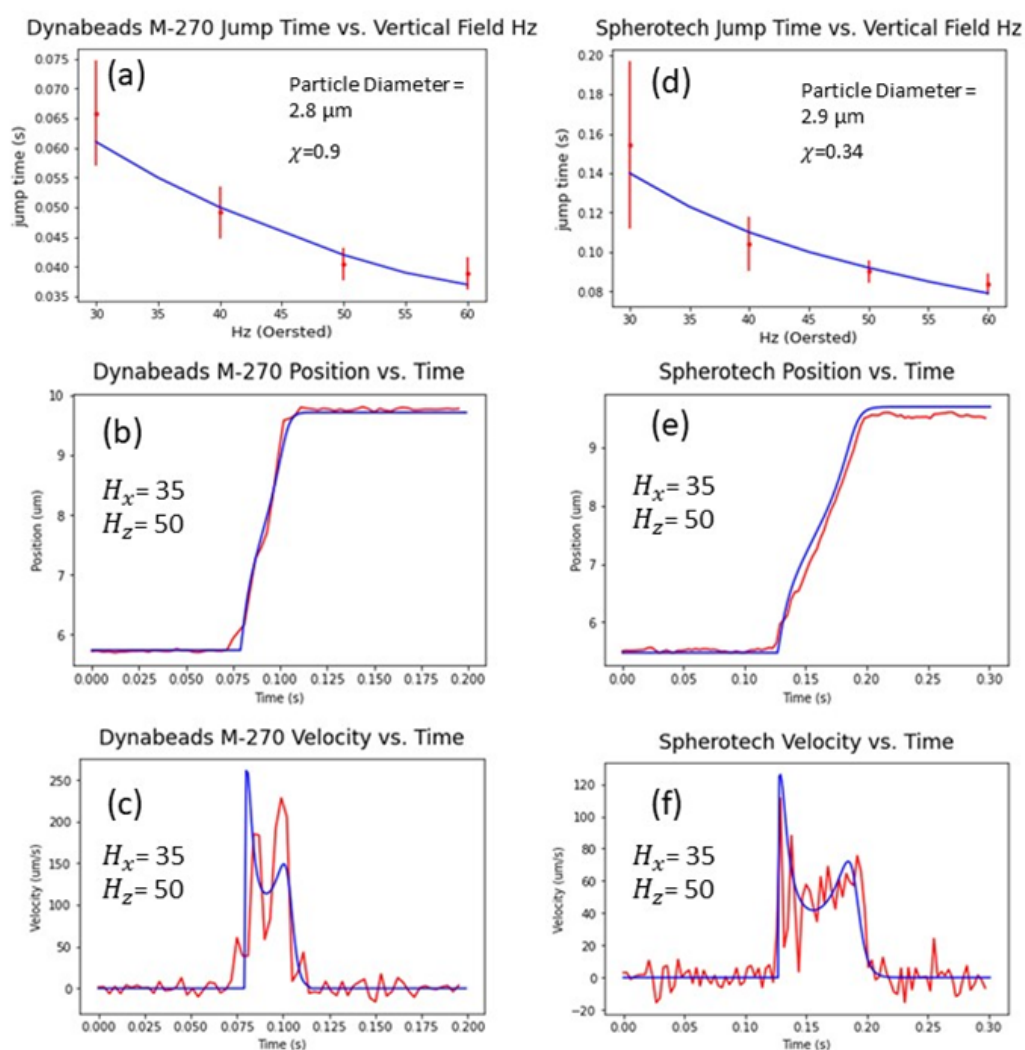


Figure 4. Short-range hopping. (a,d) Jump time decreases with H_z . Error bars calculated from the standard deviation of jump times for 10 s of jumps. (b,c,e,f) Position and velocity vs. time for disk-to-disk jumps. Blue curves are from the simulation; orange/red from the experiment. Particles are Dynabeads M-270 and Spherotech PMS-20-10.

2.2. Long Range

With a bead surface density of approximately 25 to 50 microparticles per $100 \mu\text{m} \times 100 \mu\text{m}$ square, particles were guided left or right across disk arrays using different external field frequencies. Examples are shown in Videos S2 and S3 in the supplementary material. A particle tracking routine was used to measure the average particle speed over several (at least five) cycles of magnetic field. Particles which adhered to the surface and were completely immobile were ignored. As seen in Figure 5a, the particle speed increased

linearly with the frequency up to a critical frequency of approximately 3 Hz. Motion was still observed beyond this critical frequency, but the average speed decreased. The manipulated particles (and shown in Videos S2 and S3) varied in size, and Figure 3a only reports motion for particles between 4 and 5 μm in diameter.

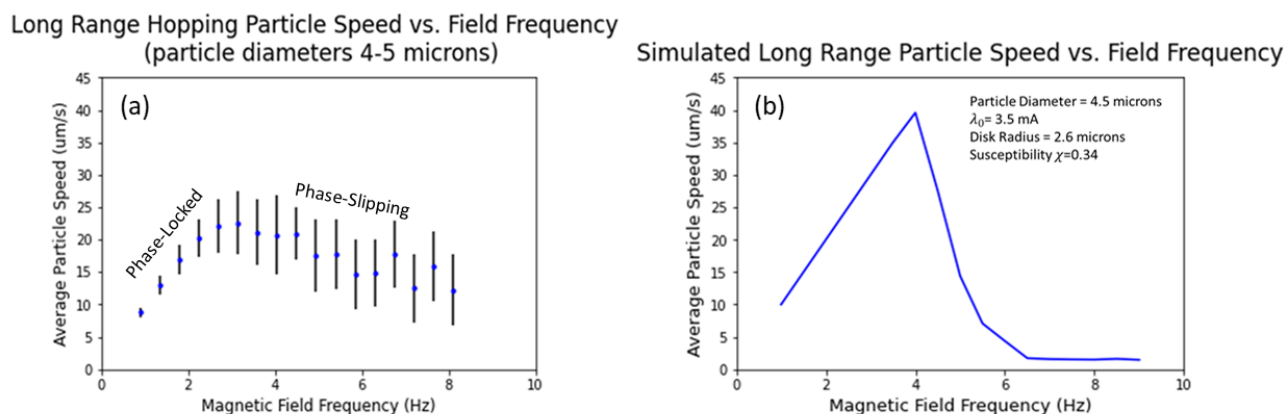


Figure 5. (a) Average particle speed as transported on the permalloy disk array. The particles used are Spherotech PMS-40-10. From 0 to 3 Hz, the motion is phase-locked, and beyond 3 Hz, the motion is phase-slipping, as the speed no longer increases with the magnetic field frequency. (b) Simulation of the speed response of a single particle.

Figure 5b shows the predicted particle speed based on the simulation described in the materials and methods. The motion of a single particle with a magnetic susceptibility of 0.34 and diameter of 4.5 microns was modeled. An example of this model is shown in Videos S4 and S5.

3. Discussion

Our simulation is able to describe the characteristics of disk-to-disk particle hopping, for example the dependence of the hop time on the external field. Furthermore, the simulation closely predicts a critical frequency of approximately 3–4 Hz for the experimental conditions used in Figure 5a. However, the measured particle speeds in the phase-locked region do not attain the predicted velocities; for example, at 2 Hz, the ideal and simulated particle motion is 20 $\mu\text{m}/\text{s}$, but the measured velocity is $17 \pm 2 \mu\text{m}/\text{s}$. Similarly, a more precipitous drop in speed past the critical frequency (in the phase-slipping region of Figure 5a) is predicted by the simulation. This simulated drop is consistent with other reports [7,13] and is consistent with reports of a “phase-insulated” or zero motion regime at larger frequencies. However, the drop is not consistent with our data. We suspect that deviations from the simulated results are due to our model only simulating one row of disks. As seen in Video S5, a phase-slipping bead may slip off of a disk laterally to the intended motion. This is common in experiments (see Video S3), but on a two-dimensional array of disks this lost bead would be further captured and manipulated by an adjacent row of disks; this is not accounted for in our model due to limitations in the computing time. Furthermore, higher phase-slipping velocities may be due to the large surface particle density in our long-range transport experiments, as our simulation only models the transport of an individual particle. Dimers or aggregates, which are prone to phase-slipping even at low frequencies, are likely to form at large bead densities, lowering speeds in the phase-locked regions of Figure 5a. Furthermore, the large densities of particles that are all magnetized by a uniform out-of-plane magnetic field lead to bead–bead magnetic repulsion [16], and bead movement does induce bulk flow [17], suggesting reasons for the lack of a fall-off in velocity in Figure 4a. We suspect that repeating experiments at lower particle densities or for individual particles would more closely match the simulation in Figure 5b. However, we suspect that a real-life application of this technique may employ

a large bead density so as to guide many particles simultaneously, and so we choose to report the data as presented.

We have investigated magnetic bead trapping and transport on disk arrays for a method of particle manipulation involving bead capture, rotation, and controlled repulsion. We have measured bead velocities during the controlled repulsion portion of the particle transport and compared the short-range bead motion to a model based on magnetic fields emanating from disk edges, suggesting that this model is able to predict measurable properties of bead motion and response to external fields. Furthermore, we have observed particle motion for long-range, multiple-disk transport, and we observe phase-locked and phase-slipping behavior. We further note that beads are not as immobile at higher field frequencies as is expected, suggesting a necessary experimental consideration when using magnetic beads on disk arrays.

4. Materials and Methods

4.1. Device Preparation

Magnetic disk arrays (Figure 1a,b) were patterned using electron beam lithography (FEL, Hillsboro, OR, USA). A silicon dioxide wafer was spin-coated at 4000 rpm with a layer of 950 PMMA C4 e-beam resist (MicroChem Corp., Newton, MA, USA) and baked for 90 s at 180 degrees Celsius. After pattern exposure using the electron microscope (with a surface dose of 300 microcoulombs/cm²), the exposed e-beam resist was developed and washed away with 1:3 methyl isobutyl ketone:isopropyl alcohol for 1 min. Following lithography, 40-nm permalloy (Ni_{0.8}Fe_{0.2}) was sputtered followed by acetone liftoff. After liftoff, disks were protected by spin-coating a 200-nm layer of spin-on glass (Futurrex IC1-200, Franklin, NJ, USA).

4.2. Experimental Methods for Particle Manipulation

Particles were suspended at a concentration of $6 \times 10^{+7}$ beads/mL in deionized water with 0.05% triton x-100 (by volume) (Triton™ X-100, Sigma Aldrich). For all experiments, the patterned surface was placed on a platform under the microscope objective lens (Figure 1c), and 5 μ L of particle solution was pipetted onto the surface, using a Polydimethylsiloxane (PDMS) o-ring to stabilize the fluid. For each experiment, a cover slip was placed over the o-ring. The platform was surrounded by four electromagnets (Magnetech OP-1212, Novi, Michigan, USA), used to generate tunable in-plane magnetic fields parallel to the surface of the platform, denoted H_{xy} (or H_x and H_y , if referring to the individual components of the field). A wire coil surrounds the platform and produces tunable out-of-plane magnetic fields, denoted H_z (Figure 1b).

The short-range particle hopping experiments initially occurred with the fields H_x and H_z set to magnitudes of a few tens of Oersted and with H_y set to zero. This caused particles to align on the same side of magnetic disks (Figure 1c). Then, the H_z direction was switched (after a 10 ms delay in which $H_z = 0$), which caused the particles to hop to a neighboring disk, as seen in Figure 2a. The subsequent reversal of H_z hopped the particle back to the initial disk, and this process was repeated (Video S1).

The long-range particle hopping experiments occurred with fields rotating 180° in the xy-plane to rotate the particle around the disk's periphery while an out-of-plane z-field was applied. This was followed by the switching of the z-field, causing particles to hop to adjacent disks. Subsequent transport was caused by a further 180° field rotation in the opposite direction and a z-field flip. The field frequency, mentioned in Figures 2 and 5, was defined in such a way that the oscillatory period was the time between consecutive H_z flips. All externally applied magnetic fields in this study were 60 Oe or less.

All experiments were performed at 22 degrees Celsius.

4.3. Particle Tracking Methods

Experiments were imaged with a camera [ThorLabs 340M-USB, Newton, NJ, USA] at 333 frames per second. A particle tracking routine was used to measure the particle position

and velocity. Particle tracking was done using the TrackMate [18] extension of ImageJ [19] allowing for particle detection, frame-to-frame particle linking, and other particle property characterizations (i.e., size measurement). Analysis of multiple videos was done by Python script to automate the process. Care was taken during microscope experiments to keep the background intensity consistent (both from video to video and across the field of view of a single video), which aided the automaticity of particle tracking routines.

4.4. Description of Simulation

The magnetic fields and particle motion were simulated by approximating magnetic fields as either emanating from or pointing toward the periphery of magnetic disks. This was done by approximating a linear magnetic charge density that varied around disk peripheries as $\lambda(\theta) = \lambda_0 \cos(\theta - \theta_0)$ where θ is the location on the disk periphery and θ_0 is the direction of the in-plane field \vec{H}_{xy} , as the in-plane field magnetizes the disks and creates two poles. The parameter λ_0 is the strength of the source of magnetic fields (which has units of amps) and is determined from the hop time vs. external field data (Figure 4a,d). Because the disks are significantly thinner than they are wide, shape anisotropy restricts the magnetization to an in-plane direction, so the out-of-plane magnetization is not considered. The stray magnetic field from a magnetic disk at point \vec{r} is approximated using the equation:

$$\vec{H}(\vec{r}) = \frac{1}{4\pi} \int \frac{\lambda(\theta) dl}{r'^2} \hat{r}' \quad (1)$$

comparable to the equation for an electric field from a given linear (electric) charge density, where \vec{r}' is a vector from a portion of the disk periphery to \vec{r} , and the integral is evaluated around the disk periphery. Each disk has two poles at opposite edges, one acting as a source and the other acting as a sink of magnetic fields.

To calculate the forces acting on a superparamagnetic particle, the superparamagnetic particles are approximated as linearly magnetizable so that magnetization $\vec{m} = \chi V \vec{H}$, where χ is the particle's magnetic susceptibility, V is the particle's volume, and \vec{H} is the magnetic field at the center of the particle resulting from both the disks and any externally applied field. The force acting on a paramagnetic particle $\vec{F} = \mu_0 \left(\vec{m} \cdot \vec{\nabla} \right) \vec{H}$, and for a linearly magnetizable particle [4]:

$$\vec{F} = \frac{1}{2} \mu_0 \chi V \vec{\nabla} H^2 \quad (2)$$

For the simulations in this paper making comparisons to Dynabead M270 experiments, the value used for the magnetic susceptibility χ is estimated to be 0.9 based on the magnetization vs. field data (for fields under 100 Oe) reported in [20].

In addition to magnetic forces, viscous fluid forces were included in the simulation. The viscous force was calculated by:

$$F_{vis} = 32\pi\eta va/3 \quad (3)$$

for a spherical particle moving along a wall [21,22]. (η is the viscosity of the solution, a is the particle's radius, and v is the particle's speed.) For all simulations, the viscosity was 8.9×10^{-4} Pa·s, the room temperature viscosity of water.

The particles moving through water are a low-Reynolds number system, and as such the inertial effects are small compared with the drag forces. At a constant force, a 1.4- μm -diameter particle reaches 99% of terminal velocity in 500 nanoseconds. However, the simulation was run using a time-step of 1 ms, so inertial terms were ignored. A particle's velocity was calculated by balancing the equations for the magnetic force and fluid drag, and a new position was calculated at each time step. Only in-plane particle

motion is considered, so all vertical forces from gravity, buoyancy, and magnetism are ignored. In addition, thermal fluctuations and friction are not considered in the model.

Supplementary Materials: The following are available online at <https://www.mdpi.com/article/10.3390/magnetochemistry7080120/s1>, Video S1: Short Range Bead Hopping, Video S2: Phase-Locked Bead Transport, Video S3: Phase-Slipping Bead Transport, Video S4: Phase-Locked Simulation, Video S5: Phase-Slipping Simulation.

Author Contributions: Conceptualization, G.B.V.; investigation, E.H., D.H., R.S., D.A.R. and E.T.C.; data curation, E.H. and D.H.; writing—original draft preparation, G.B.V.; writing—review and editing, G.B.V., E.H. and R.S.; All authors have read and agreed to the published version of the manuscript.

Funding: This research received no external funding.

Acknowledgments: We acknowledge Felio Perez and Omar Skalli at the University of Memphis Integrated Microscopy Center (<https://www.memphis.edu/imc/> (accessed on 20 August 2021)) for their essential assistance and contributions to sample fabrication for this work. We acknowledge the work done by Glen Davis in helping build the experimental apparatus. E.H. was supported by the Rhodes College Undergraduate Research Fellowship Program and the Mac Armour Fellowship in Physics.

Conflicts of Interest: The authors declare no conflict of interest.

References

1. Zborowski, M.; Chalmers, J.J. Rare Cell Separation and Analysis by Magnetic Sorting. *Anal. Chem.* **2011**, *83*, 8050–8056. [[CrossRef](#)] [[PubMed](#)]
2. Min, H.; Jo, S.-M.; Kim, H.-S. Efficient Capture and Simple Quantification of Circulating Tumor Cells Using Quantum Dots and Magnetic Beads. *Small* **2015**, *11*, 2536–2542. [[CrossRef](#)] [[PubMed](#)]
3. Klein, S.; Müller, T.G.; Khalid, D.; Sonntag-Buck, V.; Heuser, A.-M.; Glass, B.; Meurer, M.; Morales, I.; Schillak, A.; Freistaedter, A.; et al. SARS-CoV-2 RNA Extraction Using Magnetic Beads for Rapid Large-Scale Testing by RT-QPCR and RT-LAMP. *Viruses* **2020**, *12*, 863. [[CrossRef](#)] [[PubMed](#)]
4. Yellen, B.B.; Erb, R.M.; Son, H.S.; Rodward Hewlin, J.; Shang, H.; Lee, G.U. Traveling Wave Magnetophoresis for High Resolution Chip Based Separations. *Lab Chip* **2007**, *7*, 1681–1688. [[CrossRef](#)] [[PubMed](#)]
5. Henighan, T.; Chen, A.; Vieira, G.; Hauser, A.J.; Yang, F.Y.; Chalmers, J.J.; Sooryakumar, R. Manipulation of Magnetically Labeled and Unlabeled Cells with Mobile Magnetic Traps. *Biophys. J.* **2010**, *98*, 412–417. [[CrossRef](#)] [[PubMed](#)]
6. Hu, X.; Abedini-Nassab, R.; Lim, B.; Yang, Y.; Howdysshell, M.; Sooryakumar, R.; Yellen, B.B.; Kim, C. Dynamic Trajectory Analysis of Superparamagnetic Beads Driven by On-Chip Micromagnets. *J. Appl. Phys.* **2015**, *118*, 203904. [[CrossRef](#)] [[PubMed](#)]
7. Li, P.; Gandhi, D.; Mutas, M.; Ran, Y.-F.; Carr, M.; Rampini, S.; Hall, W.; Lee, G.U. Direct Identification of the Herpes Simplex Virus UL27 Gene through Single Particle Manipulation and Optical Detection Using a Micromagnetic Array. *Nanoscale* **2020**, *12*, 3482–3490. [[CrossRef](#)] [[PubMed](#)]
8. Vieira, G.; Henighan, T.; Chen, A.; Hauser, A.J.; Yang, F.Y.; Chalmers, J.J.; Sooryakumar, R. Magnetic Wire Traps and Programmable Manipulation of Biological Cells. *Phys. Rev. Lett.* **2009**, *103*, 128101. [[CrossRef](#)] [[PubMed](#)]
9. Yellen, B.B.; Virgin, L.N. Nonlinear Dynamics of Superparamagnetic Beads in a Traveling Magnetic-Field Wave. *Phys. Rev. E* **2009**, *80*, 011402. [[CrossRef](#)] [[PubMed](#)]
10. Pease, C.; Wijesinghe, H.S.; Etheridge, J.; Pierce, C.J.; Sooryakumar, R. Magnetic and Hydrodynamic Torques: Dynamics of Superparamagnetic Bead Doublets. *J. Magn. Magn. Mater.* **2018**, *466*, 323–332. [[CrossRef](#)]
11. Sajjad, U.; Holländer, R.B.; Klingbeil, F.; McCord, J. Magnetomechanics of Superparamagnetic Beads on a Magnetic Merry-Go-Round: From Micromagnetics to Radial Looping. *J. Phys. D Appl. Phys.* **2017**, *50*, 135003. [[CrossRef](#)]
12. Klingbeil, F.; Block, F.; Sajjad, U.; Holländer, R.B.; Deshpande, S.; McCord, J. Evaluating and Forecasting Movement Patterns of Magnetically Driven Microbeads in Complex Geometries. *Sci. Rep.* **2020**, *10*, 8761. [[CrossRef](#)] [[PubMed](#)]
13. Rampini, S.; Li, P.; Gandhi, D.; Mutas, M.; Ran, Y.F.; Carr, M.; Lee, G.U. Design of Micromagnetic Arrays for On-Chip Separation of Superparamagnetic Bead Aggregates and Detection of a Model Protein and Double-Stranded DNA Analytes. *Sci. Rep.* **2021**, *11*, 5302. [[CrossRef](#)] [[PubMed](#)]
14. Dynabeads Nucleic Acid Purification Support—Getting Started—US. Available online: [//www.thermofisher.com/us/en/home/technical-resources/technical-reference-library/nucleic-acid-purification-analysis-support-center/dynabeads-nucleic-acid-purification-support/dynabeads-nucleic-acid-purification-support-getting-started.html](https://www.thermofisher.com/us/en/home/technical-resources/technical-reference-library/nucleic-acid-purification-analysis-support-center/dynabeads-nucleic-acid-purification-support/dynabeads-nucleic-acid-purification-support-getting-started.html) (accessed on 19 June 2021).
15. Email Communication with Spherotech Technical Specialist. Available online: <https://www.spherotech.com/> (accessed on 19 October 2020).
16. Prikockis, M.; Chen, A.; Byvank, T.; Vieira, G.B.; Peters, B.; Yang, F.; Sooryakumar, R. Programmable Self-Assembly, Disassembly, Transport, and Reconstruction of Ordered Planar Magnetic Micro-Constructs. *IEEE Trans. Magn.* **2014**, *50*, 1–6. [[CrossRef](#)]

17. Henighan, T.; Giglio, D.; Chen, A.; Vieira, G.; Sooryakumar, R. Patterned Magnetic Traps for Magnetophoretic Assembly and Actuation of Microrotor Pumps. *Appl. Phys. Lett.* **2011**, *98*, 103505. [[CrossRef](#)]
18. Tinevez, J.-Y.; Perry, N.; Schindelin, J.; Hoopes, G.M.; Reynolds, G.D.; Laplantine, E.; Bednarek, S.Y.; Shorte, S.L.; Eliceiri, K.W. TrackMate: An Open and Extensible Platform for Single-Particle Tracking. *Methods* **2017**, *115*, 80–90. [[CrossRef](#)] [[PubMed](#)]
19. Schneider, C.A.; Rasband, W.S.; Eliceiri, K.W. NIH Image to ImageJ: 25 Years of Image Analysis. *Nat. Methods* **2012**, *9*, 671–675. [[CrossRef](#)]
20. Li, P.; Kilinc, D.; Ran, Y.-F.; Lee, G.U. Flow Enhanced Non-Linear Magnetophoretic Separation of Beads Based on Magnetic Susceptibility. *Lab Chip* **2013**, *13*, 4400–4408. [[CrossRef](#)] [[PubMed](#)]
21. Hu, X.; Goudu, S.R.; Torati, S.R.; Lim, B.; Kim, K.; Kim, C. An On-Chip Micromagnet Frictionometer Based on Magnetically Driven Colloids for Nano-Bio Interfaces. *Lab Chip* **2016**, *16*, 3485–3492. [[CrossRef](#)]
22. Hu, X.; Torati, S.R.; Yoon, J.; Lim, B.; Kim, K.; Kim, C. Magnetically Characterized Molecular Lubrication between Biofunctionalized Surfaces. *ACS Appl. Mater. Interfaces* **2018**, *10*, 16177–16182. [[CrossRef](#)] [[PubMed](#)]